Journal of Thermal Analysis and Calorimetry, Vol. 93 (2008) 3, 963–971

EFFECT OF MECHANICAL GRINDING ON THE REACTION PATHWAY AND KINETICS OF THE THERMAL DECOMPOSITION OF HYDROMAGNESITE

N. Koga and Y. Yamane*

Chemistry Laboratory, Graduate School of Education, Hiroshima University, 1-1-1 Kagamiyama, Higashi-Hiroshima 739-8524, Japan

Effect of mechanical grinding of hydromagnesite on the reaction pathway and kinetic behaviors of the thermal decomposition process was investigated by means of thermoanalytical techniques, together with crystallographic and morphological measurements. A crystalline hydromagnesite, the as-received sample, was decomposed in two distinguished mass loss steps of overlapped dehydration-dehydroxylation and dehydroxylation–decarbonation via an amorphous intermediate of carbonate compound. Thermal decomposition of an amorphous hydromagnesite, obtained by mechanical grinding of the as-received sample, was characterized by three well-separated decomposition processes of dehydration, dehydroxylation and decarbonation. The kinetic behaviors of the respective decomposition steps were estimated separately using a mathematical deconvolution of the partially overlapped reaction steps. From the formal kinetic analyses of the respective reaction processes, it was revealed that the dehydration and dehydroxylation processes indicate the decelerate rate behaviors controlled by diffusion, while the rate behavior of nucleation limited type is predominant for the decarbonation process.

Keywords: *hydromagnesite, kinetics, mechanical grinding, reaction pathway, thermal decomposition*

Introduction

Thermal decomposition of hydromagnesite, $4MgCO_3 \cdot Mg(OH)_2 \cdot 4H_2O$, have been subjected to thermoanalytical studies for revealing the reaction pathway and kinetic mechanism [1–10]. Many of these studies focused on the abrupt exothermic peak observed during the thermal decomposition process [1–6, 10] as is shown in Fig. 1, which is observed when heating the sample under relatively high partial pressure of atmospheric or self-generated CO_2. It was revealed by Sawada *et al.* [1–5] that the exothermic effect results from the crystallization of $MgCO_3$ from amorphous intermediate. The accompanied sharp increase of mass loss rate was explained by the self-heating effect due to the crystallization [1–5] and fragmentation of reacting particles by the mechanical stress [10].

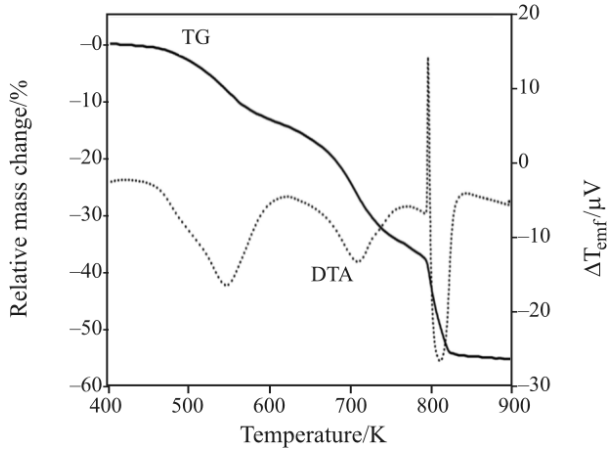

Fig. 1 Typical TG-DTA curves for the thermal decomposition of crystalline hydromagnesite (the as-received sample: 5.0 mg) in a pin-hole cell at a heating rate of 5 K min^{-1}

The reaction pathway of the thermal decomposition of hydromagnesite has been described by the following three reaction steps of dehydration, dehydroxylation and decarbonation [8].

$$4MgCO_3 \cdot Mg(OH)_2 \cdot 4H_2O \rightarrow \rightarrow 4MgCO_3 \cdot Mg(OH)_2 + 4H_2O \quad (1)$$

$$4MgCO_3 \cdot Mg(OH)_2 \rightarrow 4MgCO_3 + MgO + H_2O \quad (2)$$

$$4MgCO_3 \rightarrow 4MgO + 4CO_2 \quad (3)$$

As is shown in Fig. 2, overlapped features of the respective reaction steps were clearly seen from the measurements of TG-MS [11], where evolution of water vapor after the completion of decarbonation step was observed, in addition to partial overlapping of dehydration–dehydroxylation and dehydoxylation–decarbonation processes. Because of such overlapped reaction behaviors, kinetics of the respective reaction processes has not fully been revealed in a rigorous way. Within the very limited examples of the kinetic studies of the thermal decomposition of hydromagnesite, Rao and Chohan [9]

* Author for correspondence: nkoga@hiroshima-u.ac.jp

1388–6150/$20.00

Akadémiai Kiadó, Budapest, Hungary
Springer, Dordrecht, The Netherlands

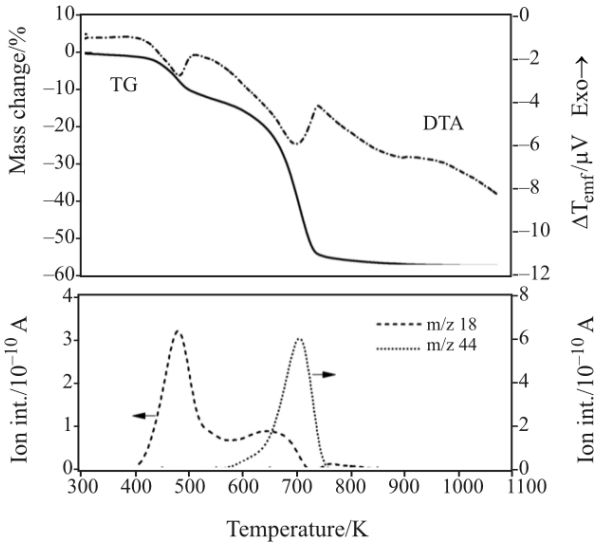

Fig. 2 Typical TG/DTA-MS curves for the thermal decomposition of crystalline hydromagnesite (the as-received sample: 2.0 mg) in an open pan at a heating rate of 10 K min^{-1} under flowing He (200 cm^3 min^{-1})

have investigated the kinetics as the reaction in two steps, i.e. dehydration and decarbonation, on the basis of the isothermal measurements for overall decomposition processes and a single nonisothermal measurement using TG. From empirical curve fitting of the experimental data in integral form, they concluded that both the dehydration and decarbonation reactions are governed by the contracting sphere mechanism with the apparent activation energies of 26.7 and 161 kJ mol^{-1}, respectively.

Among the wide varieties of industrial applications of hydromagnesite, processing of MgO powders with special morphological characteristics, such as monodispersed, nanosized, porous, and so on, via the thermal decomposition of hydromagnesite are of great interest for the advanced applications of MgO powders [12–15]. For realizing the desired properties of the solid product of the thermal decomposition, morphology control of the precursor particles is very important in order to regulate the thermal decomposition processes and the properties of the product solid, MgO [12–15]. Further detailed characterizations of the thermal decomposition pathway and kinetics are also required for controlling the morphologies and physico-chemical properties of the intermediate compounds and final solid product, MgO.

Systematic examinations of influences of the crystallinity of the reactant hydromagnesite and the reaction atmosphere on the thermal decomposition processes were subjected to the present series of studies. In this paper, the effect of mechanical grinding [16] of the reactant on the reaction pathway and kinetics of the thermal decomposition processes is reported as the first part of the studies.

Experimental

Sample preparation and characterization

Reagent grade of hydromagnesite (SAJ), $4MgCO_3 \cdot Mg(OH)_2 \cdot 4H_2O$, was used as received for the starting sample of the mechanical grinding. Morphology of the as-received hydromagnesite was observed by a scanning electron microscope (Hitachi S-2460N). A 1.5 g of the sample was weighed into 45 cm^3 alumina jar, together with seven alumina balls (ϕ=12 mm). Mechanical grinding was carried out using planetary mill (Fritsch P-7) at a rotation speed of 700 rpm for 1, 2, 3, 6, 12, 18 and 24 h. Every 30 min the rotation direction was reversed and every 1 h the grinding was stopped to scrape the sample from the balls and jars.

The as-received and ground samples were characterized by powder XRD, FTIR and TG-DTA. XRD patterns and FTIR spectra were recorded using instruments of Rigaku RINT2200V (monochrome CuK_α, 40 kV, 20 mA) and Shimadzu FTIR8100M (diffuse reflectance method), respectively. TG-DTA measurements were carried out using a ULVAC TGD9800 where the samples of ca. 5.0 mg were heated linearly at a heating rate of 5 K min^{-1} under flowing N_2 at a rate of 100 cm^3 min^{-1}. Characteristics of the sample particles were revealed by the measurements of specific surface area and particle size distribution. The specific surface areas of the samples were measured by a single point method of BET using FlowSorbII-2300 (Micromeritics). Particle size distributions of the samples were evaluated using a laser diffraction particle size analyzer (Shimadzu SALD-300V) by dispersing the sample particles in distilled water with a small amount of surfactant.

Characterization of thermal decomposition processes

Thermal decomposition processes of the sample ground mechanically for 24 h were compared with the as-received sample through various thermoanalytical measurements. TG-DTA measurements were carried out at various heating rates from 2.0 to 10.0 K min^{-1} under the conditions otherwise identical to the above TG-DTA measurements for characterizing the samples. Sample controlled TG [17] was measured using a hanging type TG (Shimadzu TGA-50) coupled with a self-constructed controller [18]. Using ca. 5.0 mg of samples weighed onto a platinum cell (6 mmϕ and 4 mm in height), the sample was heated at 5 K min^{-1} under flowing N_2 at 80 cm^3 min^{-1}, where the mass loss rate during the thermal decomposition were regulated at a constant rate of 5 μg min^{-1}. About 2.0 mg of samples weighed onto a platinum cell (5 mmϕ and 2.5 mm in height) were subjected to the measurements of TG/DTA-MS. Using an instrument of TG/DTA-MS

constructed by coupling a TG-DTA (Rigaku TG8120) with a quadrupole mass spectrometer (Anelva M-200QA), TG-DTA curves were recorded on heating at 10 K min^{-1} under flowing He (200 cm^3 min^{-1}), accompanied by continuous measurements of the mass spectra of the evolved gases (mass range: 10~50 amu, EMSN: 1.0 A, SEM: 1000 V).

Phase changes during the thermal decomposition of the samples were followed using the above described XRD instrument by equipping with a programmable heating chamber (Rigaku PTC-20A). By heating the samples at a linear heating rate of 5 K min^{-1} under flowing N_2 at 100 cm^3 min^{-1}, XRD patterns were measured at various temperatures where the sample temperature was kept constant during the diffraction measurements. Characterizations of the sample particles at several selected decomposition stages were performed by the measurements of specific surface area and particle size distribution.

Results and discussions

Changes of sample characteristics by mechanical grinding

A typical SEM image of the as-received sample is shown in Fig. 3, where aggregate of scale-like crystallites is observed. Figure 4 shows typical TG-DTA curves for the as-received sample at a heating rate of 5 K min^{-1} under flowing N_2 (100 cm^3 min^{-1}). The thermal decomposition proceeds in two distinguished mass loss steps overlapped partially, where total mass loss of 56.4±1.0 % is fairly in good agreement to the value calculated for Eqs (1)–(3), 56.9%. It is also noted that, under the conditions selected in the present study, the reaction advances smoothly without indicating the abrupt exothermic effect and rapid mass loss during the decarbonation process as was seen in Fig. 1.

Changes of the XRD patterns and FTIR spectra of the as-received sample due to mechanical grinding are shown in Figs 5 and 6, respectively. All the XRD

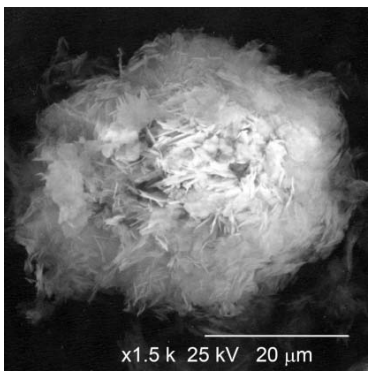

Fig. 3 A typical SEM image of the as-received hydromagnesite

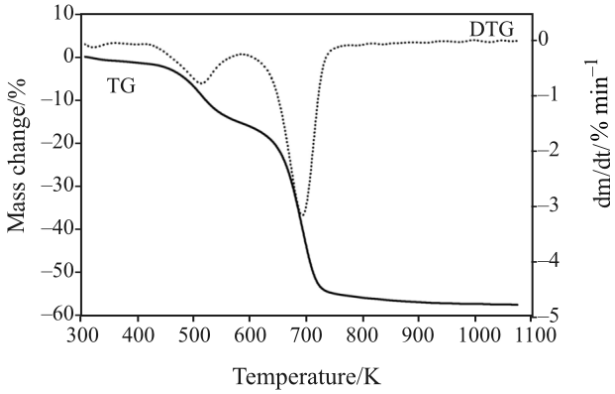

Fig. 4 Typical TG-DTG curves for the thermal decomposition of the as-received sample (5.0 mg) in an open pan at a heating rate of 5 K min^{-1} under flowing N_2 (100 cm^3 min^{-1})

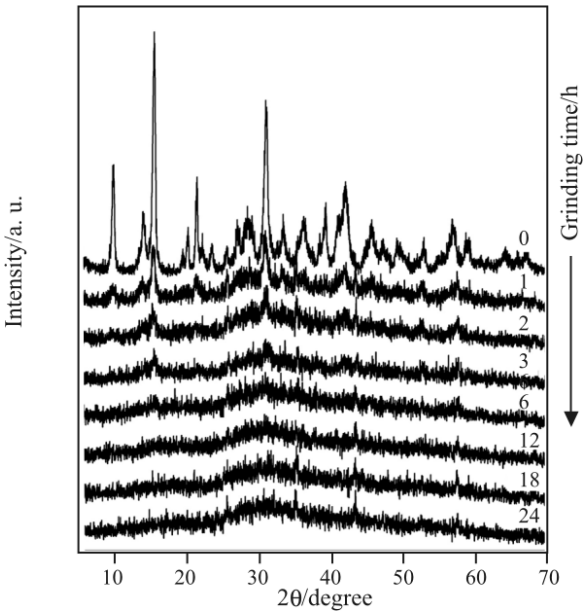

Fig. 5 Changes of the powder XRD patterns during the mechanical grinding of the as-received sample

peaks of the as-received sample correspond to that of hydromagnesite [19]. By the mechanical grinding in a planetary mill, the XRD peaks due to hydromagnesite were attenuated gradually and no distinguished diffraction peaks could be found for the samples ground for more than 12 h. Destruction of the crystal structure by the mechanical grinding is also confirmed by the broadening of all the characteristic IR absorption peaks of the as-received sample such as O–H stretching vibration (~3650 cm^{-1}), vibration of crystalline water (~3450 cm^{-1}), two split bands of ν_3 symmetric stretching vibration of carbonate ion (~1420–1490 cm^{-1}), three split bands of ν_1 stretching vibration of carbonate ion (~800, 855, 885 cm^{-1}), and so on [20, 21].

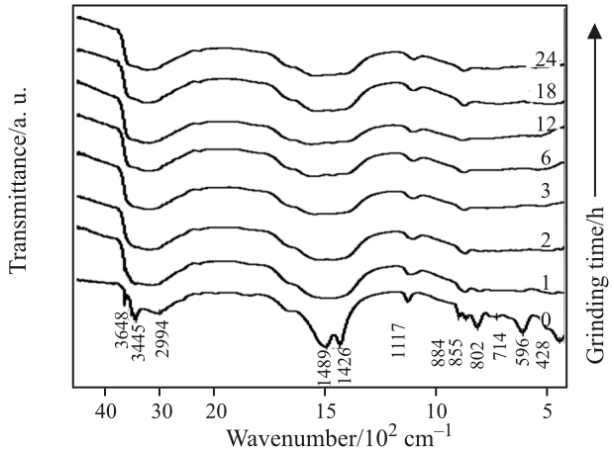

Fig. 6 Changes of the FTIR spectra during the mechanical grinding of the as-received sample

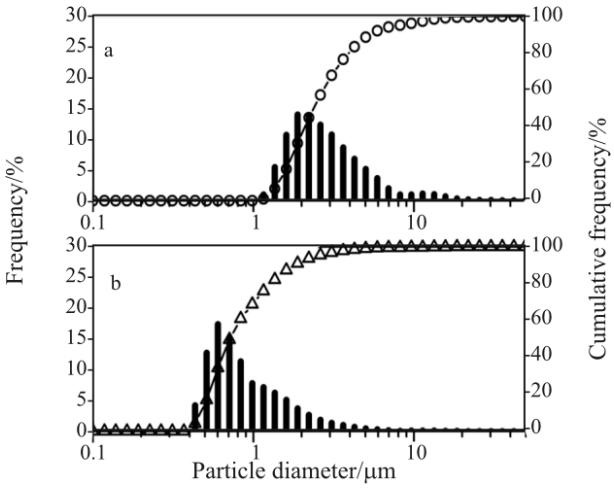

Fig. 7 Particle size distributions of the a – as-received sample and b – the sample ground for 24 h

Figure 7 compares the particle size distribution of the as-received sample and the sample ground for 24 h. The averaged particle size decreases from 2.632±0.241 to 0.835±0.246 μm by the mechanical grinding for 24 h. Unexpected decrease in the specific surface area from 22 to 8 m^2 g^{-1} were observed being contrary to the apparent decrease in the particle size, as was shown in Fig. 8. This seems to be due to the active surfaces of the finely ground sample particles being easily condensed [22].

Changes of thermal decomposition pathway

Figure 9 shows influences of the grinding time on the TG-DTG curves recorded at a heating rate of 5 K min^{-1} under flowing N_2 (100 cm^3 min^{-1}). The DTG peak for the first mass loss step of the as-received sample, characterized as the overlapped reactions of dehydration and dehydroxylation, is attenuated with mechanical

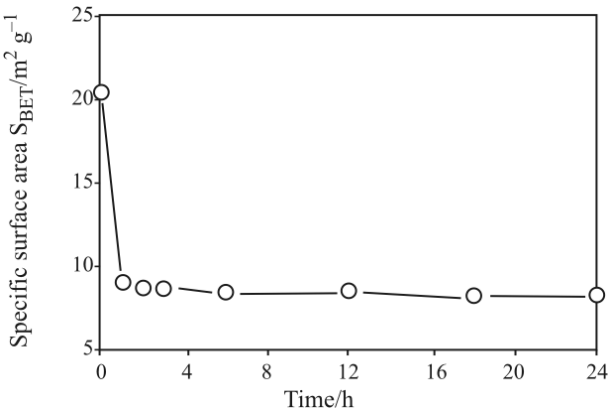

Fig. 8 Changes of the specific surface area during mechanical grinding of the as-received sample

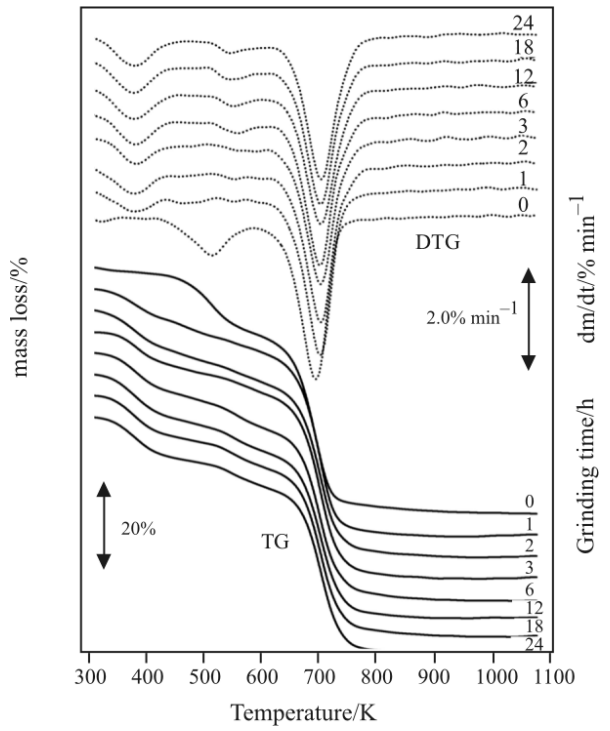

Fig. 9 Changes of TG-DTG curves of the as-received sample with the grinding time

grinding. Instead, two separated DTG peaks in the temperature ranges of 300–450 and 500–600 K appear for the samples ground for more than 6 h. The peak area of the second DTG peak of the as-received sample, characterized as the overlapped reactions of dehydroxylation and decarbonation, decreases gradually with increasing the grinding time, which is accompanied by the shift of peak top temperature from 690.8 K for the as-received sample to 700.9 K for the sample ground for 24 h. Accordingly, the thermal decomposition of the samples ground for more than 6 h proceeds via three separated reaction steps, where the averaged mass loss values of the respective reaction steps are

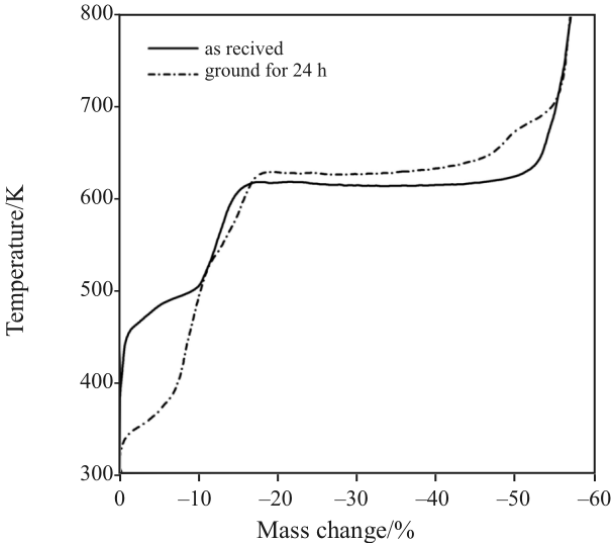

Fig. 10 Temperature profiles of constant rate TG for the thermal decomposition of the as-received sample and the sample ground for 24 h recorded at a constant mass loss rate of 5.0 μm min^{-1} under flowing N_2 (100 cm^3 min^{-1})

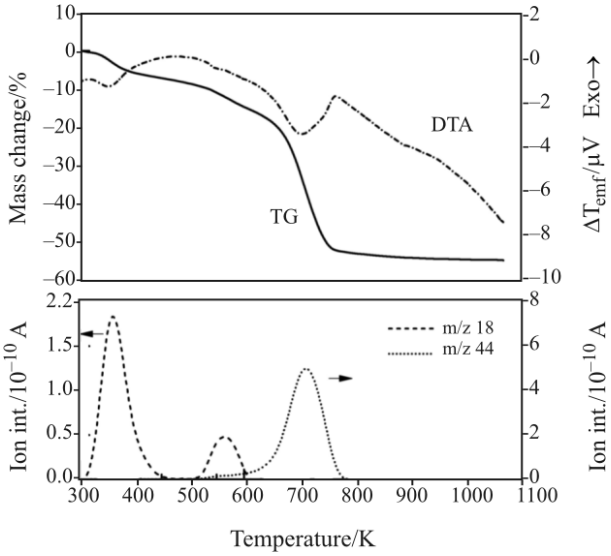

Fig. 11 Typical TG-DTA curves and mass chromatograms of evolved gases during the thermal decomposition of the sample ground for 24 h (2.0 mg) at a heating rate of 10 K min^{-1} under flowing He (200 cm^3 min^{-1})

13.2±0.7, 4.7±0.4, and 38.3±1.2 % which are closely corresponding to the calculated values for Eqs (1)–(3), 15.4, 3.8 and 37.6%.

Figure 10 compares the temperature profiles of the constant rate thermal decomposition of the as-received sample and the sample ground for 24 h. It is clearly seen that the two different reaction temperature ranges observed for the as-received sample are separated into three distinguished ranges by the mechanical grinding. Such change of reaction steps results from the remarkable fall of the dehydration temperature which is likely due to the destruction of crystal structure. It is also noted that the reaction temperature of decarbonation, observed as the third reaction step of the ground sample, is slightly higher than that of the as-received sample. Further, under the condition of constant rate decomposition, an additional reaction step is observed at the end of the decarbonation reaction.

Figure 11 shows TG-DTA curves and mass chromatograms of the evolved gases during the thermal decomposition of the sample ground for 24 h. In comparison with those for the as-received sample shown in Fig. 2, the processes of H_2O evolution are separated clearly into two different steps in the ground sample. The process of CO_2 evolution is also separated from that of H_2O. The above results indicate that the mechanical grinding of the sample promotes the separation of the respective reaction steps of dehydration, dehydroxylation, and decarbonation as expressed by Eqs (1)~(3).

Changes of the powder XRD patterns during the course of thermal decomposition were shown in Fig. 12.

The as-received sample, i.e. crystalline hydromagnesite, decomposes via an intermediate amorphous phase produced during the first mass loss step of overlapped dehydration and dehydroxylation. Through the second mass loss step of overlapped dehydroxylation and decarbonation processes, MgO crystallized as the solid product of the thermal decomposition of the amorphous intermediate. Such phase change behaviors during the thermal decomposition of the as-received sample are in good agreement with those reported previously by Sawada *et al*. [2]. As for the ground sample which is amorphous in view of XRD, no distinguished XRD peak appears during the first mass loss step of separated dehydration. On further heating, weak diffraction peaks of $MgCO_3$ [23] and $MgO{\cdot}2MgCO_3$ [24] appear during the second mass loss step of separated dehydroxylation. Thus, the third mass loss step of decarbonation takes place as the thermal decomposition of mixed carbonates of amorphous intermediate, $MgCO_3$ and $MgO{\cdot}2MgCO_3$, which explains the shift of reaction temperature of decarbonation process of the ground sample to higher temperature as was observed in Figs 9 and 10. The diffraction peaks of $MgCO_3$ and $MgO{\cdot}2MgCO_3$ are observed until the final stage of the decarbonation process. Therefore, it is very likely that the additional reaction step observed at the end of the decarbonation process of the ground sample under the condition of constant rate decomposition is due to the thermal decomposition of such crystalline carbonates. For both the samples, the XRD peaks due to final product MgO [25] grow with further heating.

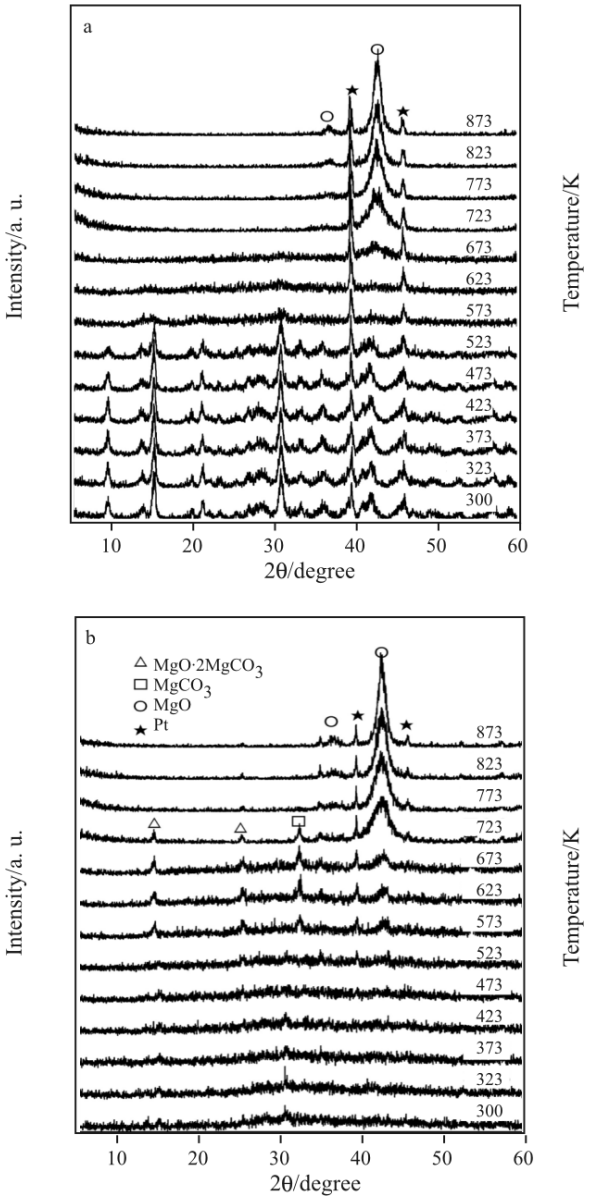

Fig. 12 Changes of the powder XRD patterns of during the thermal decomposition of the a – as-received sample and b – the sample ground for 24 h

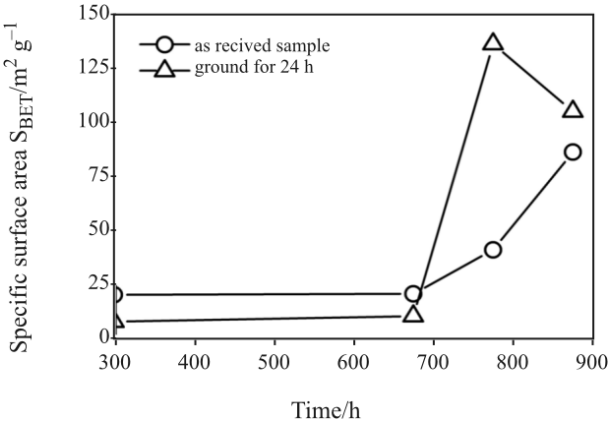

Fig. 13 Changes of the specific surface area during the thermal decomposition processes of the as-received sample and the sample ground for 24 h

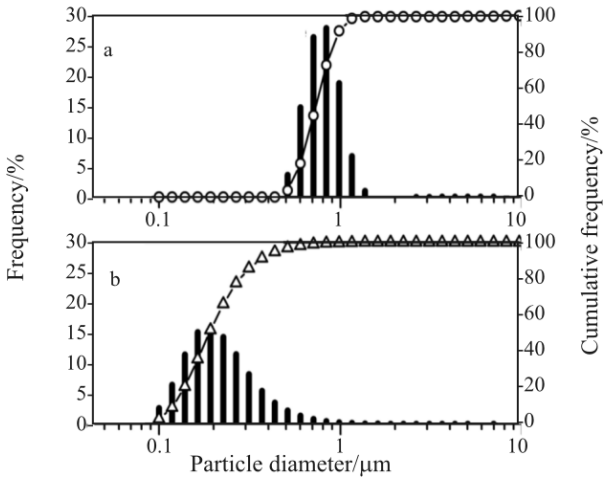

Fig. 14 Particle size distributions of the decomposition products at 773 K of the a – as-received sample and b – the sample ground for 24 h

Figure 13 shows changes of the specific surface area of the as-received and ground samples during the thermal decomposition processes. At the end of the decarbonation processes, 773 K, a large difference of the specific surface areas can be seen between the as-received and ground samples, in spite of the comparable intensity and half-width of the XRD peaks due to MgO observed in this temperature region, Fig. 12. Particle size distributions of the as-received and ground samples heated to 773 K are compared in Fig. 14. The averaged particle size and standard deviation for the as-received and ground samples at 773 K are 0.743±0.128 and 0.189±0.191 μm, respectively. On further heating to 873 K, the specific surface areas of the as-received and ground samples increases and decreases, respectively, indicating comparable values around 100 cm^2 g^{-1}. A possible interpretation for the above observations seems to be given in relation to the differences in the physico-geometric mechanisms of the decarbonation reaction and crystallization of MgO. As for the as-received sample, the product crystallites of MgO are produced in the matrix of amorphous intermediate, so that the characteristics of product particles at 773 K are inherited largely from the amorphous intermediate. The increase in the specific surface area on further heating indicates the destruction of the amorphous matrix induced by the crystal growth of MgO. On the other hand, finely dispersed particles of MgO are produced during the decarbonation process of the ground sample. On further heating, the specific surface area decreases

due to the crystal growth of MgO particles. Detailed microscopic studies are now in progress for verifying the assumptions on the physico-geometric mechanisms of the decarbonation reaction.

Kinetic characterization of the respective decomposition steps

In order to obtain the kinetic rate data for the separated reaction steps of dehydration, dehydroxylation and decarbonation, DTG curves for the ground sample were subjected to a mathematical peak deconvolution using Lorentz function. Figure 15 shows the deconvoluted DTG curves for the respective reaction steps, together with the original DTG curve at a heating rate of 5 K min^{-1}. Using the separated DTG curves at different heating rates as the kinetic rate data, the apparent activation energies, E_a, for the respective reaction steps were determined by Friedman method [26] at various selected fractional reactions α, according to the following equation.

$$\ln\frac{d\alpha}{dt}=\ln[Af(\alpha)]-\frac{E_a}{RT} \quad (4)$$

where A and $f(\alpha)$ are the pre-exponential factor and kinetic model function, respectively. Such Friedman plots, $\ln(d\alpha/dt)$ *vs.* T^{-1}, at α=0.5 were shown in Fig. 16. For all the reaction steps, good linear plots of $\ln(d\alpha/dt)$ *vs.* T^{-1} with the correlation coefficient $-\gamma>0.98$ were obtained in fairly wide range of α. Table 1 lists the values of E_a for the respective reaction steps averaged over selected ranges of α where the slopes of the Friedman plots indicated acceptably constant.

By extrapolating the isoconversional relationships of Friedman plots to infinite temperature, isothermal rate behaviors of the respective reaction steps were reproduced at infinite temperature. At a selected α, the reaction rate at infinite temperature, expressed as

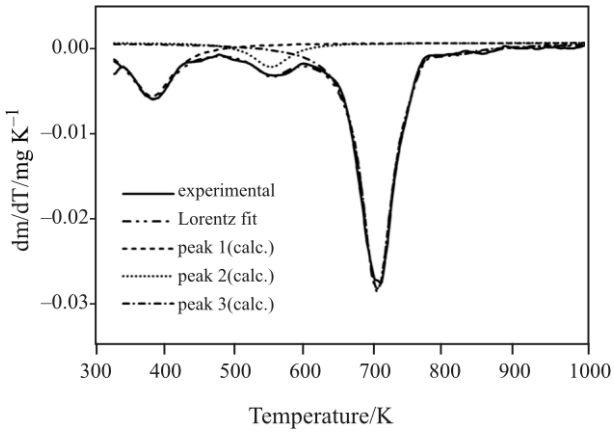

Fig. 15 Deconvolution of DTG curve for the thermal decomposition of the sample ground for 24 h at a heating rate of 5 K min^{-1}

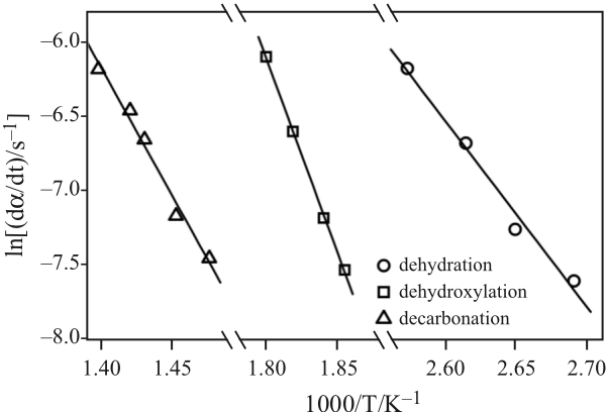

Fig. 16 Friedman plots at α=0.5 for the respective reaction processes of the thermal decomposition of the sample ground for 24 h

Table 1 The values of E_a for the respective reaction steps averaged over selected ranges of α

Reaction step	Range of α	E_a/kJ mol^{-1}	Error
Dehydration	0.10≤α≤0.75	89±6	6±1
Dehydroxylation	0.20≤α≤0.65	216±6	13±4
Decarbonation	0.20≤α≤0.75	141±7	5±1

$(d\alpha/d\theta)$ using the Ozawa's generalized time θ [27–29], is calculated using the measured rate data $(d\alpha/dt, T)$ and experimenetal value of E_a [30, 31].

$$\frac{d\alpha}{d\theta}=\frac{d\alpha}{dt}\exp\left(\frac{E_a}{RT}\right) \quad (5)$$

The isothermal rate behavior at infinite temperature, $(d\alpha/d\theta)$ *vs.* α, is related to the kinetic model function $f(\alpha)$ by the equation [30, 31].

$$\frac{d\alpha}{d\theta}=Af(\alpha) \quad (6)$$

Defining a reference point at α=0.5, Eq. (6) is converted to Eq. (7) [32, 33].

$$\frac{(d\alpha/d\theta)}{(d\alpha/d\theta)_{0.5}}=\frac{f(\alpha)}{f(0.5)} \quad (7)$$

On the basis of Eq. (7), an appropriate type of $f(\alpha)$ characterized the physico-geometric behavior of the reaction can be selected through comparing the theoretical master plot, $f(\alpha)/f(0.5)$ *vs.* α, with the experimental master plot, $(d\alpha/d\theta)/(d\alpha/d\theta)_{0.5}$ *vs.* α.

Figure 17 illustrates the experimental master plots for the respective reaction steps, together with the theoretical master plots for the three-dimensional diffusion controlled (D3) model, $f(\alpha)=3(1-\alpha)^{2/3}/2[1-(1-\alpha)^{1/3}]$, and the first-order (F1) model, $f(\alpha)=1-\alpha$. The experimental master plots for the dehydration and dehydroxylation processes are

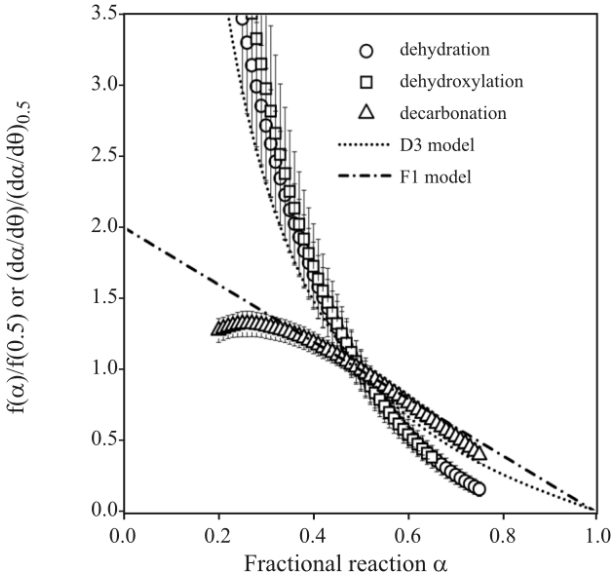

Fig. 17 The experimental master plots for the respective reaction processes of the thermal decomposition of the sample ground for 24 h

practically identical indicating the rate behavior of diffusion controlled type. Thus the separation of the reaction steps of dehydration and dehydroxylation by the mechanical grinding is interpreted by the decrease in the E_a value for the dehydration process due to the destruction of crystalline structure of hydromagnesite, Table 1. The experimental master plot for the decarbonation process indicates the maximum at α= 0.25 and subsequently decelerates linearly. The linear decelerate process is apparently fitted to the theoretical master plot of F1 model, which indicates the rate behavior limited by the nucleation of solid product. Such nucleation limited behavior supports the formation of finely dispersed MgO particles during the decarbonation process of the ground sample, as was deduced from the large specific surface area of the solid product.

Conclusions

- Under relatively low partial pressure of CO_2 during the course of reaction, the thermal decomposition of a well-crystalline hydromagnesite, i.e. the as-received sample, was characterized by two separated mass loss steps of overlapped dehydration-dehydroxylation and dehydroxylation-decarbonation via an amorphous intermediate phase of carbonate compounds.
- By grinding mechanically the crystalline hydromagnesite, an amorphous hydromagensite was obtained. The amorphous hydromagnesite decomposed through three well-separated mass loss steps of dehydration, dehydroxylation and decarbonation. During the thermal dehydration process, no distinguished crystalline phase was produced. Poorly crystallized phases of $MgCO_3$ and $MgO{\cdot}2MgCO_3$ were produced during the dehydroxylation process. The decarbonation takes place by the thermal decomposition of a mixture of intermediate amorphous phase and poorly crystalline carbonates, $MgCO_3$ and $MgO{\cdot}2MgCO_3$, where the crystalline carbonates decomposed at the final stage of the decarbonation process.
- The kinetic behaviors of the dehydration and dehydroxylation processes were characterized by the diffusion controlled type reaction with the apparent values of E_a=89±6 and 216±6 kJ mol^{-1}, respectively. On the other hand, the nucleation limited reaction with E_a=141±7 kJ mol^{-1} was estimated for the decarbonation reaction.

Acknowledgements

The present work was supported partially by a grant-in-aid for scientific research (B) (No. 18300267) from Japan Society for the Promotion of Science.

References

1 Y. Sawada, K. Uematsu, N. Mizutani and M. Kato, J. Inorg. Nucl. Chem., 40 (1978) 979.
2 Y. Sawada, K. Uematsu, N. Mizutani and M. Kato, Thermochim. Acta, 27 (1978) 45.
3 Y. Sawada, J. Yamaguchi, O. Sakurai, K. Uematsu, N. Mizutani and M. Kato, Thermochim. Acta, 32 (1979) 277.
4 Y. Sawada, J. Yamaguchi, O. Sakurai, K. Uematsu, N. Mizutani and M. Kato, Thermochim. Acta, 33 (1979) 127.
5 Y. Sawada, J. Yamaguchi, O. Sakurai, K. Uematsu, N. Mizutani and M. Kato, Thermochim. Acta, 34 (1979) 233.
6 C. Padeste, H. R. Oswald and A. Reller, Mater. Res. Bull., 26 (1991) 1263.
7 G. Helou and S. A. Tariq, Thermochim. Acta, 228 (1993) 123.
8 V. R. Choudhary, S. G. Pataskar, V. G. Gunjikar and G. B. Zope, Thermochim. Acta, 232 (1994) 95.
9 T. R. Rao and V. S. Chohan, Chem. Eng. Technol., 18 (1995) 359.
10 N. Khan, D. Dollimore, K. Alexander and F. W. Wilburn, Thermochim. Acta, 367/368 (2001) 321.
11 Y. Sawada, Mater. Integr., 12 (1999) 65, in Japanese.
12 S. A. Morozov, A. A. Malkov and A. A. Matygin, Russ. J. Gen. Chem., 73 (2003) 41.
13 S. A. Morozov, A. A. Malkov and A. A. Matygin, Russ. J. Gen. Chem., 76 (2003) 7.
14 Q. Li, Y. Ding, G. Yu, C. Li, F. Li and Y. Qian, Solid State Commun., 125 (2003) 117.
15 J. Y. Kim, H. S.Jung and K. S. Hong, J. Am. Ceram. Soc., 88 (2005) 784.
16 M. Senna, J. Therm. Anal. Cal., 90 (2007) 107.

17 O. T. Sorensen and J. Rouquerol, Eds, Sample Controlled Thermal Analysis. Kluwer, Dordrecht 2003.
18 N. Koga, J. M. Criado and H. Tanaka, J. Therm. Anal. Cal., 60 (2000) 943.
19 JCPDS 25-0513.
20 A. Botha and C. A. Strydom, J. Therm. Anal. Cal., 71 (2003) 987.
21 J. Lanas and J. I. Alvarez, Thermochim. Acta, 421 (2004) 123.
22 Y. Waseda and A. Muramatsu, Eds, Morphology Control of Materials and Nanoparticles, Springer, 2004.
23 JCPDS 08-0479.
24 JCPDS 31-0804.
25 JCPDS 45-0946.
26 H. L. Friedman, J. Polym. Sci. C, 6 (1964) 183.
27 T. Ozawa, Bull. Chem. Soc. Jpn., 38 (1965) 1881.
28 T. Ozawa, J. Thermal Anal., 2 (1970) 301.
29 T. Ozawa, Thermochim. Acta, 100 (1986) 109.
30 T. Ozawa, J. Thermal Anal., 31 (1986) 547.
31 N. Koga, Thermochim. Acta, 258 (1995) 145.
32 F. J. Gotor, J. M. Criado, J. Malek and N. Koga, J. Phys. Chem. A, 104 (2000) 10777.
33 J.M. Criado, L. A. Perez-Maqueda, F. J. Gotor, J. Malek and N. Koga, J. Therm. Anal. Cal., 72 (2003) 901.

Received: November 4, 2007
Accepted: January 28, 2008
OnlineFirst: June 25, 2008

DOI: 10.1007/s10973-007-8616-4